



Image-based crack assessment of bridge piers using unmanned aerial vehicles and three-dimensional scene reconstruction

Yu-Fei Liu¹ | Xin Nie¹ | Jian-Sheng Fan¹ | Xiao-Gang Liu²

¹Key Laboratory of Civil Engineering Safety and Durability of China Education Ministry, Department of Civil Engineering, Tsinghua University, Beijing, China

²Central Research Institute of Building and Construction CO., LTD., MCC Group, Beijing, China

Correspondence

Yu-Fei Liu, Key Laboratory of Civil Engineering Safety and Durability of China Education Ministry, Department of Civil Engineering, Tsinghua University, Beijing, China 100084. Email: liuyufei@tsinghua.edu.cn

Funding information

National Natural Science Foundation of China, Grant/Award Numbers: 51978376, 51725803

Abstract

Crack assessment of bridge piers using unmanned aerial vehicles (UAVs) eliminates unsafe factors of manual inspection and provides a potential way for the maintenance of transportation infrastructures. However, the implementation of UAV-based crack assessment for real bridge piers is hindered by several key issues, including the following: (a) both perspective distortion and the geometry distortion by nonflat structural surfaces usually appear on crack images taken by the UAV system from the pier surface; however, these two kinds of distortions are difficult to correct at the same time; and (b) the crack image taken by a close-range inspection flight UAV system is partially imaged, containing only a small part of the entire surface of the pier, and thereby hinders crack localization. In this paper, a new image-based crack assessment methodology for bridge piers using UAV and three-dimensional (3D) scene reconstruction is proposed. First, the data acquisition of UAV-based crack assessment is discussed, and the UAV flight path and photography strategy for bridge pier assessment are proposed. Second, image-based crack detection and 3D reconstruction are conducted to obtain crack width feature pair sequences and 3D surface models, respectively. Third, a new method of projecting cracks onto a meshed 3D surface triangular model is proposed, which can correct both the perspective distortion and geometry distortion by nonflat structural surfaces, and realize the crack localization. Field test investigations of crack assessment of a real bridge pier using a UAV are carried out for illustration, validation, and error analysis of the proposed methodology.

1 | INTRODUCTION

Coming on the heels of the large-scale infrastructure construction in China in the last 20 years, the demand for condition assessment of existing transportation infrastructures, including highway bridges, railway bridges, and municipal bridges, has rapidly increased (Ou & Li, 2010; Qarib & Adeli, 2014). Periodic and continuous assessment, and structural health monitoring can ensure the safety of transportation infrastructures according to related research achievement and summary of engineering experience (Amezquita-Sanchez &

Adeli, 2015; Vaghefi et al., 2011). However, due to safety and efficiency reasons, traditional manual routine inspection can no longer completely satisfy the requirements of practical engineering. For example, the recently built rigid frame bridges, Hezhangt Bridge and Sanshui River Bridge in China, whose piers are as high as 180 m, pose a hard problem to bridge managers—that it is extremely tough to conduct on-site manual inspection on such bridge piers. New and reliable testing and inspection methods are urgently needed.

Aiming at the structural surface crack, the image-based crack detection method has received increasing attention



in this decade. The quantifiable image-based surface crack assessment method consists of two main steps. The first step is crack detection, which intends to eliminate noise and extract crack objects from the images. The existing research on the topic of crack detection using the digital image processing (DIP) method mainly focuses on this step. The study of wavelet analysis (e.g., Jahanshahi & Masri, 2012; Sonka, Hlavac, & Boyle, 1999), background subtraction (Fujita & Hamamoto, 2011; Liu, Cho, Spencer, & Fan, 2014), mathematical methods such as morphological operation (e.g., Sinha & Fieguth, 2006) and adaptive crack template (e.g., Huang, Tian, Xu, & Xing, 2017), and edge detectors (e.g., Abdel-Qader, Abudayyeh, & Kelly, 2003), etc., offer useful tools for crack detection with their own scope of application. For bridge assessment, Yeum and Dyke (2015) proposed a very clever method for the detection of fatigue cracks near the bolts of steel beams using object detection and grouping techniques. In recent years, with the rapid advance of artificial intelligence, convolutional neural networks (ConvNets) have acted as a more and more powerful processor in the processing of digital images, as well as in the field of image-based crack detection. Cha, Choi, and Büyüköztürk (2017) designed a systematic ConvNets architecture based on deep learning to achieve image-based crack edge detection. Yang et al. (2018) proposed a more elaborate pixel-level crack detection method using a fully convolutional neural network. Besides, Wang and Hu (2017), Zhang et al. (2017), and Xu et al. (2018) conducted research on image and ConvNets-based crack detection for asphalt road surface, concrete road surface, and steel structures, respectively. Kim, Ahn, Shin, & Sim (2019) developed an efficient classification framework based on the crack candidate region and achieved differentiation of real crack and crack-like objects on the concrete surface. Recent research on surface damage classification based on the neural network method can be seen in the work of Li, Zhao, and Zhou (2019) and Maeda, Takahashi, Ogawa, and Haseyama (2019).

The second step of crack assessment is the extraction of crack edges and the calculation of crack parameters including crack width and length. Nishikawa, Yoshida, Sugiyama, and Fujino (2012) proposed a brightness-derived function to find the actual edge of the crack and define the crack width. Lee, Kim, Yi, and Kim (2013) defined the crack width to be the intersection point of the normal line of the crack skeleton and the crack edge line. Liu et al. (2014) improved Lee et al.'s method to use an eight-connected normal line to calculate the intersection point and provided crack width nephograms.

By being mounted on an unmanned aerial vehicle (UAV), the imaging device can take advantage of its remote sensing capabilities to a greater extent (Vaghefi et al., 2011). As early as a decade ago, Metni and Hamel (2007) tried a radio-controlled helicopter for bridge crack detection and provided a control law for the helicopter. However, since the radio-controlled helicopter was hard to control, and the flight path

was hence unstable, the crack assessment technology based on such equipment failed to receive enough attention until the appearance of a multicopter drone. Ellenberg, Kontos, Moon, and Bartoli (2016) tested a quadcopter for infrastructure assessment and provided a homography transformation method to correct obliquely taken crack images. Khan et al. (2015) verified the performance of infrastructure inspection using a UAV equipped with an RGB camera and an IR camera, wherein deck degradation of crack and delamination were detected. Similar studies were carried out by Sankarasrinivasan, Balasubramanian, Karthik, Chandrasekar, and Gupta (2015) and Morgenthal and Hallermann (2014). Recently, Lei, Wang, Xu, and Song (2018) proposed the crack central point method for crack detection and bridge inspection using a UAV. Reagan, Sabato, and Niezrecki (2018) combined the three-dimensional digital image correlation (3D-DIC) technique with the UAV system for the measurement of displacement and crack growth on bridges. In this research, the authors found that the movement of a UAV does not significantly affect the precision of 3D-DIC measurements. Kang and Cha (2018) adopted an ultrasonic beacon for UAV navigation during crack assessment for the first time and combined the ConvNets-based crack detection methods.

However, among the existing studies on image-based or UAV-based crack detection, little attention is paid to the deformation of cracks. In addition to the image distortion of the camera and lens, perspective distortion and the geometry distortion by nonflat structural surfaces are two important factors that cause the deformation of crack objects in the image. Perspective distortion is usually embodied as follows: the distant objects appear smaller than nearby objects of the same size in the same image. For camera A in Case 1 of Figure 1, perpendicular shooting can avoid perspective distortion but is difficult to realize during the shooting using a UAV because the flight control request is too high. The usual shooting model is camera B. Crack images obtained by camera B will have obvious perspective distortion, causing the crack shape to deform and the calculated crack width to be wrong (the distant cracks are narrower than nearby cracks of the same width).

The geometry distortion by nonflat structural surfaces is another important and commonly seen image distortion in the on-site inspection of real engineering projects. Cases 2, 3, and 4 in Figure 1 show different cases of bridge piers where cracks are propagating along a nonflat surface. The cameras C, D, and E will get crack images of obvious geometry distortion. This kind of crack distortion is commonly seen in the bridge assessment but is hard to correct by the simply use of 2D images. Furthermore, the surface of the bridge pier may be pitted and uneven, or the pier may be in a curved shape. Under such circumstances, 2D image distortion correction and large area inspection methods, such as image stitching methods (e.g., Zhu, Fu, Yang, & Zhang, 2016), may fail. The reason is that the surface of the inspection object cannot

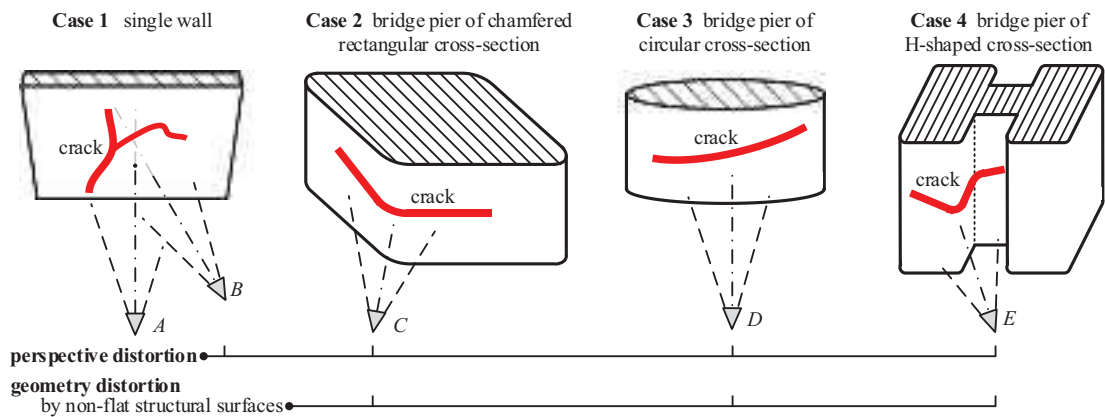


FIGURE 1 Crack image capture for different types of surfaces of structures

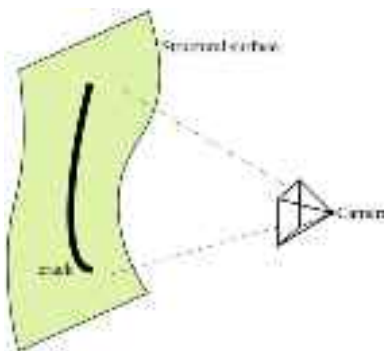


FIGURE 2 Imaging of a curved planar surface



FIGURE 3 Curved bridge pier

be unfolded into a plane at this time. For structural surfaces that are difficult to unfold, image stitching will result in errors in the depth direction, such as in the curved surface shown in Figure 2 and the actual bridge pier shown in Figure 3. The above deformation in the depth direction will result in inaccurate calculation of the crack parameters.

Besides image distortion, crack localization is another critical problem for the implementation of image-based crack detection methods. When assessing large-scale real-world structures and infrastructures, a telephoto lens for long-distance shooting or a drone for close-up shooting are reliable solutions for enlarging the views and finding small cracks. In these cases, the captured photo contains a very small scene around the crack. As illustrated in Figure 4, crack images #1

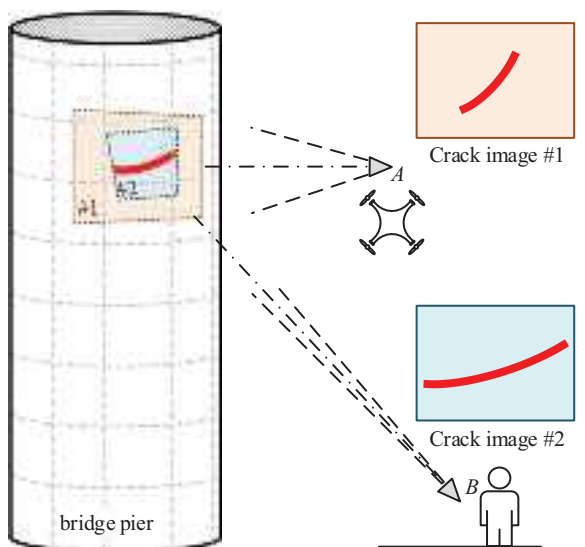


FIGURE 4 Problem of crack localization using small-view images in bridge assessment

and #2 are captured using the UAV (camera A) and the telephoto lens (camera B), respectively. Although these small-view and zoomed-in images are good for small crack detection and crack width calculation, crack localization becomes very difficult to achieve. Such small-view images contain too little information and features, making it difficult to determine the relative position of the identified crack on the surface of the structure. Similar problems exist in the on-site inspection of large-scale concrete structures such as a dam body and a nuclear containment structure. In laboratory tests and for some of the real projects, people use the method of drawing gridlines and labeling on the structure surface for crack localization, as illustrated in Figure 4. However, this method is quite impossible to conduct on large-scale structures and infrastructures.

Due to the above two problems, that is, image distortion and localization, the image-based condition assessment method using a UAV can hardly be implemented in real-world

structures and infrastructures. Aiming at the above problems, this paper proposes a new image-based crack assessment methodology for bridge piers using a UAV and 3D scene reconstruction. First, the data acquisition for UAV-based crack assessment is discussed, and the UAV flight path and photography strategy for bridge pier assessment are proposed. Second, image-based crack detection and 3D reconstruction are conducted to obtain crack width feature pair sequences and 3D surface models, respectively. Third, a new method of projecting cracks onto a meshed 3D surface triangular model is proposed, which can correct both the perspective distortion and geometry distortion by nonflat structural surfaces, and realize crack localization. Field test investigations on crack assessment on a real bridge pier using a UAV are carried out for illustration, validation, and error analysis of the proposed methodology.

2 | METHODOLOGY FRAMEWORK OF THIS PAPER

The proposed methodology in this paper contains five parts: image data acquisition, crack detection using digital images, image-based 3D reconstruction, crack projection, and field test. The framework is presented in Figure 5. In detail, image data acquisition is about the flight path of a UAV and photography strategy during the inspection of bridge piers. Crack projection is to project the crack feature point detected in the 2D digital images onto the 3D triangular surface model. The main contributions of this paper are image data acquisition, crack projection, and error analysis, which are marked with dashed boxes in Figure 5. The other two parts, crack detection and image-based 3D reconstruction, are modular subroutines

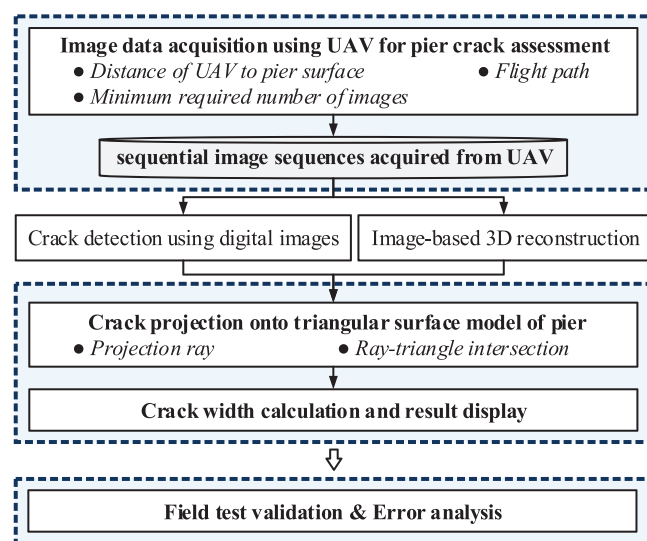


FIGURE 5 Methodology framework and contribution of this paper

throughout the whole methodology and employ the existing mature methods.

3 | IMAGE DATA ACQUISITION

3.1 | Distance of a flying UAV from the structure surface

Because the camera lens mounted on the UAV is usually a prime lens with a fixed focal length, the distance from the flying UAV to the structure surface determines the size of the imaging scene and the width of the narrowest detectable crack. Therefore, by using the thin lens model shown in Figure 6, the physical width of the detectable crack is calculated as follows:

$$W_r = \frac{W_p}{P_c} \cdot \frac{u}{v} \quad (1)$$

where W_r and W_p refer to the crack width in the units of millimeters and pixels, respectively; P_c refers to the ppmm (pixel per millimeter) of the camera sensor (e.g., CMOS or CCD); u , v refer to the working distance and the image distance, respectively. Moreover, u and v are controlled by the thin lens model as follows:

$$\frac{1}{u} + \frac{1}{v} = \frac{1}{f} \quad (2)$$

where f refers to the focal length.

According to the present algorithms, the narrowest detectable crack should contain at least 1 or 3 pixels along the width direction on the image. The corresponding working distance can be calculated using Equations (1) and (2).

3.2 | Flight path and photography strategy

What needs to be known before acquiring the image sequence for damage inspection using a UAV is where to shoot and when to shoot, that is, the flight path of a UAV and the photography strategy. The requirements of the obtained image sequence include the following: (a) at least 50% overlap of each adjacent image is needed to conduct image-based scene 3D reconstruction and (b) the working distance should be

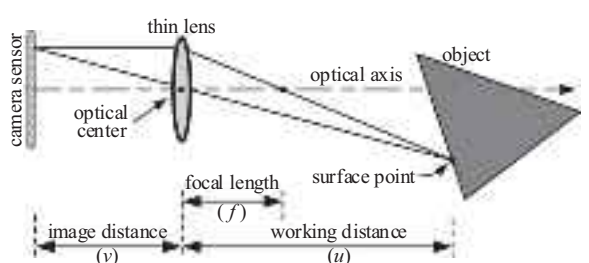


FIGURE 6 Thin-lens model



well controlled to ensure that the crack images have sufficient resolution for the narrowest cracks. In this subsection, UAV flight paths for the inspection of bridge piers with a round section, square section, rectangular section, and chamfered rectangular section are studied. The flight paths for circular and chamfered rectangular sections are designed and discussed corresponding to the bridge piers mentioned.

3.2.1 | Flight path for a circular section

For bridge piers with a round section, square section, rectangular section, and chamfered rectangular section, the most simple flight path of the UAV for inspection is circular. When discussing the working distance of a camera on a flying UAV, square, rectangular, and chamfered rectangular cross-sections of bridge piers are simplified and replaced by their excircles. The radius of the excircles and the radius of the round pier section are all the same and defined as r , as illustrated in Figure 7. In this figure, the excircle of the three sections is overlapped with the round pier section. The flight path of the UAV is the concentric outer circle, whose radius equals $l + r$, where l is defined as the distance from the UAV to the excircle. The following discussion is based on the assumption that the UAV system shoots the center of the bridge pier. Take the two shooting points on the flight path, P_1 and P_2 , in Figure 7, for example. Their optical axes are right towards the center and intersect the section of the round pier or the excircle of the other three kinds of piers at points Q_2 and Q_3 . The arc between point Q_2 and point Q_3 becomes the estimated overlap zone for the bridge pier. θ , γ are the central angle $\angle P_1 O P_2$, and the horizontal imaging angle of the camera, respectively.

To meet the requirements of 3D scene reconstruction and crack detection, the flight path and the photographing strategy of a UAV system should follow three principles: clear image, sufficient overlap, and sufficient resolution. The proposed measures and procedures are as follows:

1. Multiple images should be taken by the UAV system at the same shooting position to minimize blurring of the captured image.
2. Enough shooting points need to be determined on the flight path to ensure a minimum 50% overlap. The case with the 50% overlap is shown in Figure 7, where the edge of the camera view angle exactly intersects the optical axis of the next image on the surface of the bridge pier. In detail, line $P_1 Q_3$, the edge of the camera view when shooting from P_1 , intersects the optical axis $P_2 O$ when shooting from P_2 , and the intersect point is located just at point Q_3 on the surface of the round pier section. Assume that for each shooting, the central angle of the two adjacent positions of the UAV is kept as θ . Therefore, to achieve a higher overlap than 50%, one can choose a central angle smaller than θ .
3. Given the camera and lens parameters, a shorter working distance results in a higher crack detection resolution, as discussed in Section 3.1 and Equations (1) and (2). In turn, given a requested crack detection resolution, the working distance of the UAV system can be computed, and the flight path and photography strategy are obtained.

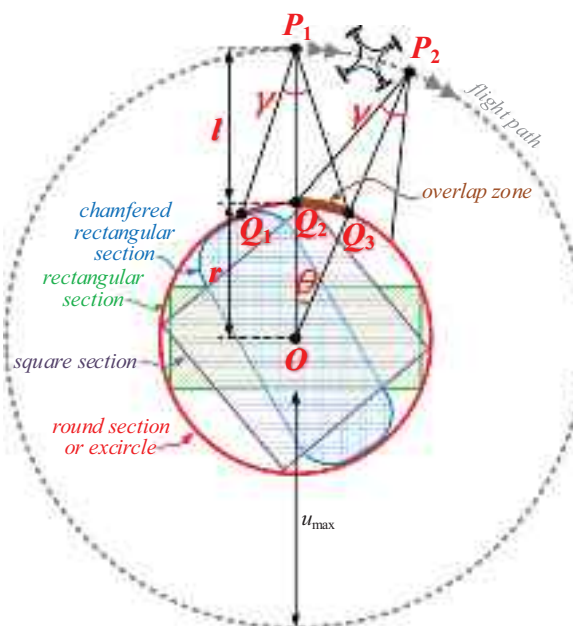


FIGURE 7 Flight path for the circular section and minimum 50% overlap

Geometric analysis is carried out using the case with a minimum 50% overlap presented in Figure 7. The relationship between l (i.e., the distance from the UAV to the excircle) and θ (i.e., the central angle) is derived and presented by Equation (3). For the case of the round pier section, l equals the working distance, u . For pier cross-sections that are square, rectangular, and rectangular with an inconspicuous chamfer, the working distance varies when the UAV moves on the circular path. The maximum working distance appears when shooting towards the midpoint of the long side of the square pier. Here, the crack detection resolution is the worst, which is regarded as the control resolution. In this case, the value of l can be computed using Equation (4), where λ is defined as the ratio of the lengths of the long side to the short side of the pier section; u_{\max} represents the maximum working distance. After θ is obtained, the number of shots of a UAV flying a lap, which is defined as N_r , can be computed using Equation (5). In short, to meet the requirements of sufficient crack detection resolution and image overlap, the important parameters of the flight path and the photographing strategy



of a UAV system, that is, θ , N_r , and u , are obtained by combining Equations (1)–(5).

$$\begin{cases} \theta = \arcsin \left[\left(1 + \frac{l}{r} \right) \sin \frac{\gamma}{2} \right] - \frac{\gamma}{2}, & \text{when } l \leq \frac{r}{\sin(\frac{\gamma}{2})} - r \\ \theta = \frac{\pi}{2} - \arcsin \left(\frac{r}{l+r} \right), & \text{when } l > \frac{r}{\sin(\frac{\gamma}{2})} - r \end{cases} \quad (3)$$

$$l = u_{\max} - r \left(1 - \frac{1}{\sqrt{1 + \lambda^2}} \right) \quad (4)$$

$$N_r = \left\lceil \frac{2\pi}{\theta} \right\rceil \quad (5)$$

3.2.2 | Flight path for a chamfered rectangular section

For bridge piers with a rectangular section and chamfered rectangular section, the ratio of the lengths of the long side to the short side of the pier section (i.e., λ) may be a bit large. Here, the flight path for a circular section is not that applicable because the working distance of the camera varies too much while flying. In contrast, the flight path for the chamfered rectangular section presented in Figure 8 is more suitable. The parameters of the flight path and the photographing

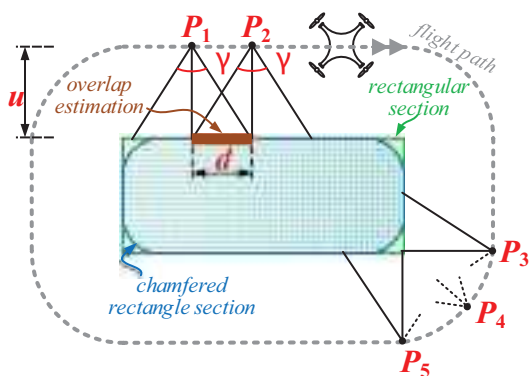


FIGURE 8 Flight path for the chamfered rectangular section and minimum 50% overlap

strategy, that is, u and d , respectively, can be obtained by combining Equations (1), (2), and (6). Similar to the former case of the circular flight path, the overlap of adjacent images is 50%, such as that from the shooting points P_1 and P_2 presented in Figure 8. To achieve higher overlap than 50%, one can choose a lateral translation distance for the UAV shorter than d . In addition, at the corner of the flight path, shooting three or more images is sufficient for the requirement of 3D reconstruction. Note that when the UAV is moving in a straight line along the sides of the rectangle section, the shot images will be parallel to each other, resulting in a larger area of the region of uncertainty (Rashidi, Dai, Brilakis, & Vela, 2013), which may ultimately degrade the quality of the 3D reconstruction. Therefore, a little oblique photography and denser shooting are recommended here.

$$d = u \cdot \tan \frac{\gamma}{2} \quad (6)$$

3.3 | Illustrative example

Here, the cameras of Canon EOS 5D Mark III (hereinafter referred to as 5D III) and DJI Zenmuse X5S (hereinafter referred to as X5S) are taken as examples to illustrate the calculation of working distance and number of shots. The former camera can be mounted on the DJI UAV of S1000+ or M600, and the latter Inspire 2. The focal length selected for 5D III is 35 mm, and for X5S is 15 mm and 45 mm. All the selected lenses are commonly used wide-angle prime lenses for UAV photography. The bridge pier used for the illustrative example is a circular cross-section with a radius of 1.5 m. The results of the width of the narrowest crack detectable and the number of shots needed during one circular flight are presented in Figure 9. The width of the narrowest detectable crack is computed under the assumption that a 1-pixel width crack is the minimum.

For a crack width of 1 mm, the working distance needed is no more than 5.64 m for 5D III with a focal length of 35 mm, 4.41 m for X5S with a focal length of 15 mm, and 13.23 m for

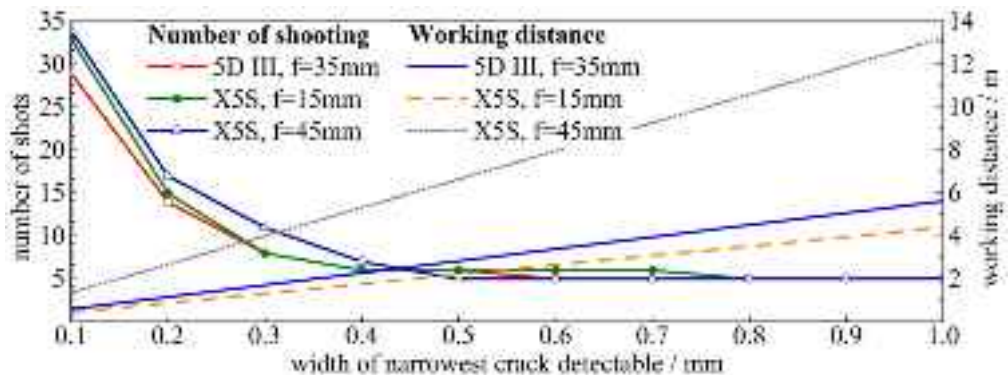


FIGURE 9 Relationship between the working distance, the number of shots, and the width of the narrowest crack detectable



X5S with a focal length of 45 mm. The corresponding number of shots is 5 in total. These results of the working distance and number of shots are quite acceptable for practical application. For cracks wider than 1 mm, the needed working distance becomes longer, and the number of shots remains the same.

For a crack width of 0.1 mm, the working distance needed is no more than 0.60 m for 5D III with a focal length of 35 mm, 0.45 m for X5S with a focal length of 15 mm, and 1.36 m for X5S with a focal length of 45 mm. The corresponding number of shots is 29, 33, and 34, respectively. Notice that a working distance shorter than 1.00 m will be hard to achieve because it is difficult to operate a UAV to stay so close to the surface of the pier. In this situation, lenses of longer focal length are needed.

4 | CRACK DETECTION AND 3D RECONSTRUCTION

Crack detection based on DIP and 3D scene reconstruction of the bridge piers is conducted after acquiring image data from on-site inspection using a UAV. The former step is to identify the necessary parameters of crack objects, that is, the crack width feature pair; the last step is to recover the 3D triangular mesh model for the bridge piers, which will be used in the projection process.

4.1 | Crack detection and crack width feature pair extraction

In this paper, adaptive crack detection and parameter extraction methods based on 2D images proposed by Liu et al. (2014) are employed. The process of adaptive crack detection includes image subtraction with a median filter and Niblack's local binarization. Here, the optimal filter size index is employed to simultaneously select the optimal window size of the median filter and the binarization operator, thereby minimizing noise and enhancing the crack objects. The process of crack parameter extraction includes crack decomposition, edge detection of crack segments, and crack parameter extraction. The crack width on 2D images is defined as the distance between two intersection pixels on the normal line of the skeleton line and those on two edge lines, as shown in Figure 10.

However, as discussed, cracks in the 2D images may contain distortion and could be unusable to obtain the crack shape and crack width directly. In this paper, the important crack feature points are projected back to the 3D model. Afterward, the crack shape is obtained and the crack width is computed. The important crack feature points to be projected are named the crack width feature pair, which are stored in a sequence in the following format: [crack segment ID,



FIGURE 10 Important crack feature points

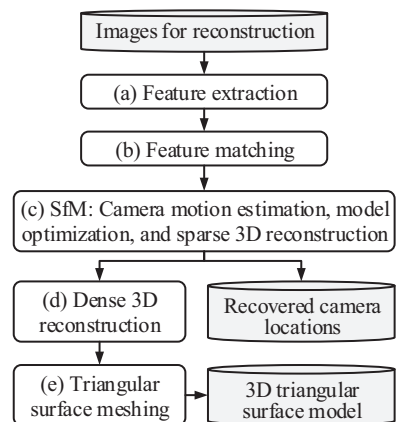


FIGURE 11 Flow diagram of the process of 3D scene and surface reconstruction

coordinates of left crack width point, coordinates of crack skeleton point, coordinates of right crack width point].

4.2 | Three-dimensional scene and surface reconstruction

Three-dimensional scene reconstruction from multiple images is a classic and challenging problem in the area of computer vision (Zisserman, 2003), with many intercrossed applications such as structural damage detection (Adhikari, Moselhi, & Bagchi, 2014; Khaloo, Lattanzi, Cunningham, Dell'Andrea, & Riley, 2018; Yang et al., 2018). Because of its advantages of low cost and ease of use, the image-based 3D reconstruction method has been considered an alternative to traditional 3D modeling methods such as 3D laser scanning.

The main process of image-based 3D reconstruction is shown in Figure 11, where the inputs are images for reconstruction and outputs are recovered camera locations and the 3D triangular surface model. In this paper, some faster and more efficient algorithms are employed rather than the classic and traditional algorithms, as presented in Table 1. For example, in the process of feature extraction and matching,



TABLE 1 Methods employed in the process of three-dimensional (3D) scene and surface reconstruction

Steps of image-based 3D reconstruction	Employed methods
(a) Feature extraction	KAZE features by Alcantarilla, Bartoli, and Davison (2012)
(b) Feature matching	Cascade hashing by Cheng, Leng, Wu, Cui, and Lu (2014)
(c) Structure from motion	ACSFm by Moulon, Monasse, and Marlet (2012)
(d) Dense 3D reconstruction	PatchMatch by Barnes, Shechtman, Finkelstein, and Goldman (2009)
(d) Triangular surface meshing and refinement	Surface reconstruction and refined mesh by Jancosek and Pajdla (2014) and Vu, Labatut, Pons, and Keriven (2012)

KAZE features by Alcantarilla, Bartoli, and Davison (2012) are adopted instead of the commonly used and classic scale invariant feature transform proposed by Lowe (2004). For another example—the mesh refinement algorithm is added to the triangular surface meshing step to ensure that the generated triangular surface model has higher quality, thereby further improving the accuracy of the crack projection. Commonly used commercial 3D reconstruction software usually does not include the triangular mesh refinement algorithm.

The steps of feature extraction (KAZE), feature matching (cascade hashing), and structure from motion (ACSFm) are implemented by openMVG (<https://github.com/openMVG/openMVG>) using C++, while the steps of dense 3D reconstruction (PatchMatch), and triangular surface meshing and refinement are implemented by openMVS (<https://github.com/cdcseacave/openMVS>) using C++. The generated recovered camera locations and refined 3D triangular surface model will be utilized in the crack projection process described hereinafter.

It should be noted that because the point cloud is discrete and nonuniform, neither the dense 3D point cloud model nor the triangular surface model can be used in crack detection directly. Information of crack width feature pairs such as crack skeleton points may not just be included in the point cloud.

5 | CRACK PROJECTING ONTO A TRIANGULAR SURFACE MODEL

Crack projection is to project the crack width feature pair sequence from 2D images back onto the recovered 3D triangular surface model using the thin lens model (Figure 6). One of the most important motivations of the projection process is to correct both the perspective distortion and the geometry distortion by nonflat structural surfaces. The projection methods

proposed by Liu, Cho, Spencer, and Fan (2016) are developed on in this paper. By this method, the crack width feature pair detected in 2D images is projected onto fitted 3D planes. It is known that the recovered 3D model by SfM is a discontinuous point cloud model. Before projection, the point cloud model has to be transferred to a kind of continuous surface model in order to compute the projecting intersection points. In the method by Liu et al. (2016), procedures of “plane fitting on the 3D scene cloud” and “determination of crack planes using proximal key points” are executed before projection. For a flat structural surface that contains only one or several planes, the idea of plane fitting works. For structures of complex geometry contour and nonflat surfaces such as curved surfaces or concave surfaces, the method of plane fitting fails because the fitted planes can no longer represent the real structural surfaces elaborately.

In this paper, the crack width feature pairs are projected back onto the meshed triangular surface model. The imaging model and the computation of the projection ray are discussed in this section. Meanwhile, seeking to deal with the complex intersecting relationship of a ray against a large number of triangular patches, an effective crack collision detection integration method is developed.

5.1 | Imaging model and Projection ray

The imaging model describes the relationship between a point in space and the projection of the point on the image plane through a series of coordinate systems, which is composed of three major elements, the optical center, the image plane, and the scene. The projection ray starts from the optical center, goes through the point of the crack width feature pair sequence, and finally intersects the 3D continuous surface model. Here, the imaging model by Liu et al. (2016) is employed.

It is known that the world coordinate of the optical center is $\mathbf{R}^{-1}\mathbf{T}$. On the basis of the world coordinate equation of the crack width point given by Liu et al. (2016), the projection ray of crack width point “ p ” that starts from the optical center “ O_c ” can be obtained as:

$$\overline{O_c p} = f \mathbf{R}^{-1} \mathbf{K}^{-1} \begin{bmatrix} u \\ v \\ 1 \end{bmatrix} \quad (7)$$

where f denotes the focal length of the camera; \mathbf{R} and \mathbf{K} denote the 3×3 rotation matrix and the 3×3 calibrated camera intrinsic parameter matrix, respectively; and (u, v) denote the coordinate of point “ p ” on the pixel coordinate system.

Before projection, the preprocessing steps of camera calibration and image distortion correction, and keyframe extraction given by Liu et al. (2016) are employed.

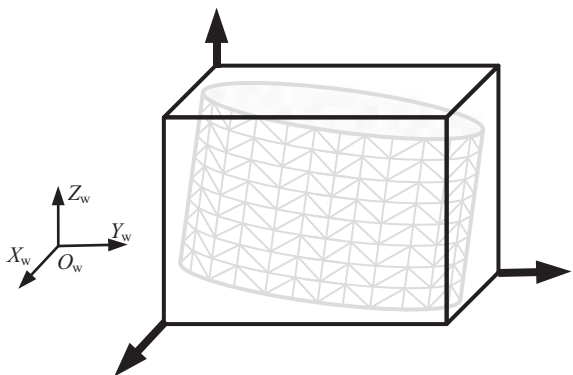


FIGURE 12 Axis aligned bounding box with a triangular surface model inside

5.2 | Collision detection and ray-triangle intersection

The projection of a crack width feature pair sequence onto the triangular surface model is a collision detection problem. During the imaging process, the unobstructed structural surfaces that are the nearest to the camera are shot. In reverse, during the projection process, the first intersection point of the ray on the triangular surface model represents its real location in the 3D scene. The second or other intersection point is on the hidden surface and not at the real location. To deal with the collision detection of numerous projection rays and a large number of triangle patches, important strategies including bounding volume, hierarchy and traversal, and ray-triangle intersection are considered, as described in the following subsections:

5.2.1 | Bounding volumes

Collision detection by checking the intersection relationship of each ray with all the triangle patches is expensive and hard to accomplish. To solve this problem, the axis aligned bounding box (AABB) (Ericson, 2004) is adopted to simplify the intersection calculation. This bounding box is a rectangular six-sided 3D box whose faces are parallel with the three axes of the world coordinate system at all times. The faces of the bounding box located at the minimum or maximum coordinate of the points of the inside patches are used to realize a tight fit using a very simple geometric shape. In this way, the collision detection of a ray and lots of triangle patches are transformed into fast overlap rejection tests of the ray and AABBs. The ray-triangle intersection is not calculated until the ray collides with the box. Figure 12 shows the illustration of an AABB containing a triangular surface model.

5.2.2 | Hierarchy and traversal

Bounding volume hierarchies are created to manage the complicated triangular patch collection of the surface model as a binary tree-type hierarchical system. The binary AABB

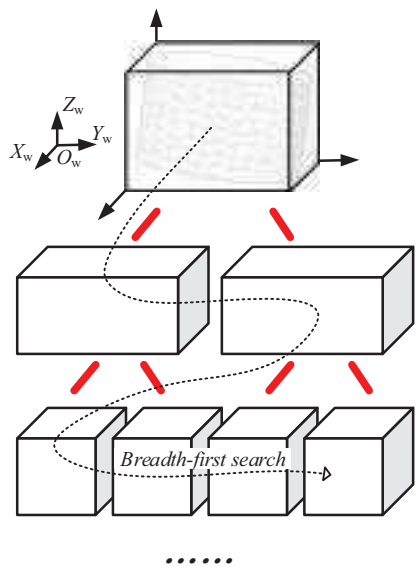


FIGURE 13 Bounding volume tree of the axis aligned bounding box

tree is built from the top down, as illustrated in Figure 13. At each subdivision step, the AABB on the parent node is partitioned into two parts and two child AABBs are created, until the AABB contains only one triangle. Breadth-first search (Figure 13) is employed for the traversal of the AABB tree in this paper. During the breadth-first search of the AABB tree, the search starts from the root of the tree and explores all the neighbor nodes from one level to the next, deeper level as a hierarchical traversal process. Only the child nodes whose parent nodes have intersections with the ray will be searched and recursively down until the leaf nodes are found. In comparison to the brute-force method, that is, searching the triangle patches one by one, the procedure of breadth-first search of the AABB tree is much faster. The computational complexity of the AABB tree and breadth-first traversal is $O(\log(n))$, where n is the number of primitives of the tree. After the search, all the leaf nodes that collide with the ray will be selected as possible intersections of the ray and triangle patches.

5.2.3 | Intersection

The intersection of the ray and the triangle is calculated only at the leaf nodes that intersect the ray. The calculation is a simple geometric problem and not discussed in this paper. The nearest intersection point of the ray-triangle and the end point of the ray will be regarded as the real projection point, which represented the point of the crack width feature pair at the real scene (Figure 14).

5.3 | Projection process

The entire projection process is illustrated in Figure 15. For the bridge pier with a cylindrical or elliptic cylindrical shape,

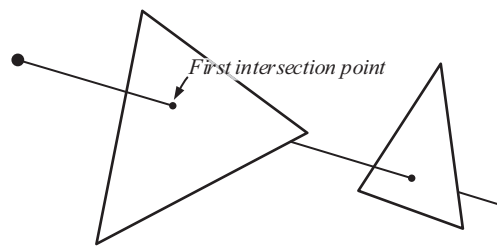


FIGURE 14 Ray-triangle intersection

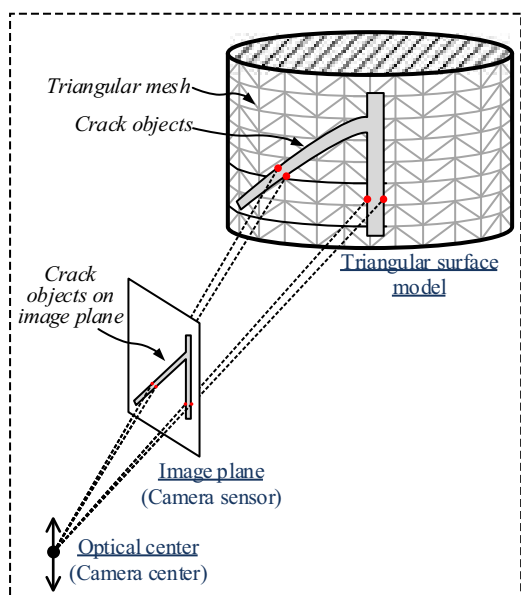


FIGURE 15 Crack projection onto a cylindrical or elliptic cylindrical surface

the crack objects on the image plane are distorted, as shown on the image plane in Figure 15. After the projection of the crack width feature pair sequence, the real crack shape and exact crack position in the 3D scene are obtained. The crack width is calculated using the 3D coordinates of the projected crack width points after model size correction using one known distance or element dimension.

In conclusion, the benefits of the projection include the following:

1. Both the perspective distortion and the geometry distortion by nonflat structural surfaces of the crack images are corrected after the projection. The nonflat structural surfaces can have any kind of surface geometry. The corrected crack objects are in real and original 3D shape, and the crack width is accurately calculated after the correction.
2. The global localization of the detected cracks is achieved, and the relative positions of the detected cracks are marked on the 3D model of the bridge pier.

3. Detection of large-area cracks is realized by projecting and stitching cracks from different images onto the same 3D model.

6 | FIELD TEST INVESTIGATIONS

UAV inspection tests of a bridge pier through image-based 3D reconstruction and crack detection are presented in this section for the illustration and investigation of the proposed methodology.

6.1 | Imaging and flight equipment and setup

The DJI Inspire 2, a professional film drone, which is easy to control and stable when flying, is employed in the field tests. An X5S camera and a prime lens are mounted on the drone. The specifications of the UAV system include: (a) weight 3.90 kg with X5S, (b) size of the camera sensor is 4/3", (c) the pixel resolution of the image is $5,280 \times 2,970$, (d) the focal length of the lens is 15 mm, (e) the minimum focus distance is 0.2 m, and (f) the GPS hovering accuracy is 1 ± 0.1 m vertically and ± 0.3 m horizontally. The tests are conducted in good weather conditions with calm winds and an appropriate temperature. A temperature that is too low will result in poor performance of the UAV battery. Meanwhile, it is recommended to arrange the on-site inspection and photography early in the morning or on cloudy days to obtain uniform solar illumination, which is what we do in these field tests. This measure is to ensure uniform brightness of the image.

6.2 | A railway bridge pier for field tests

A bridge pier on the Feng-Sha Second Railway Line (from Beijing Fengtai District to Shajia Town of Huailai County) and near the Yongding River is selected for the field test. The Feng-Sha Second Railway was built between 1959 and 1972 and has been serving for more than 46 years. The selected bridge pier is a round-ended pier whose bottom half is truncated cone-shaped, as presented in Figure 16. Several panel joints exist on the surface of the pier, and the inspection zone is selected around the panel joint #2 of the truncated cone part, as presented in Figure 16, because there are several winding curved surface cracks in the inspection zone. For these cracks, the special geometric surface shape of the pier introduces both horizontal and vertical geometry distortions when shooting. The flight path of the UAV is circular around the inspection zone, and the diameter of the pier on the plane of the flight path is 4.81 m. This diameter value is used to correct the size of the 3D model. The height of the inspection zone is about 1.0 m.

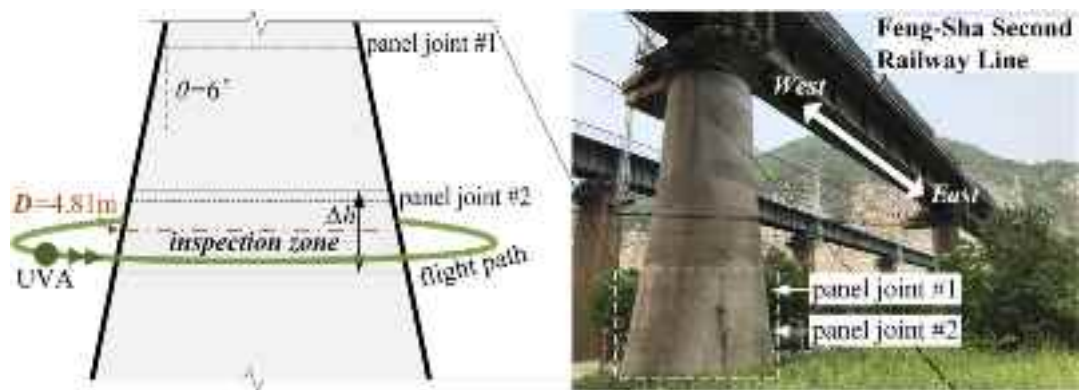


FIGURE 16 The selected bridge pier for the field test

6.3 | Test design and test parameters

The flight path of the UAV should be designed according to the request for crack assessment. According to the Chinese code for rating existing railway bridges (2014-120), the horizontal and vertical cracks of concrete piers should be checked during the on-site testing. However, this code does not provide measurement accuracy for a specific crack width. During the preliminary inspection of the selected bridge pier for the field test, it is found that the crack width varied from about 0.5 mm to 3.0 mm in the inspection zone and are possibly force cracks. The focal length and ppm of the UAV camera are 15 mm and 293 pixel/mm, respectively. Substituting the above values into Equations (1) and (2), the minimum working distance of the camera is calculated to be 748 mm when the crack that is 3 pixels in width is assumed to be the narrowest one detectable. According to the trials and experience of the drone pilot, 1.00 m may be the closest safe distance between the UAV and the pier surface. Being too close to the pier surface may lead to danger. Therefore, with comprehensive consideration of the minimum working distance and safe distance, the flight paths of the UAVs are designed with working distances of 1.00 m, 1.50 m, and 2.00 m in a circular shape. The goal of selecting three different working distances is to verify the effectiveness of the flight path design method proposed in Section 3 by varying parameters, and observe the overall effect of crack identification under different working distances.

The field operation is shown in Figure 17a, and crack width at several selected points is measured using a vernier caliper (as shown in Figure 17b) and a crack ruler. During the UAV flight, the radar map of DJI Inspire 2 and DJI GO 4 (as shown in Figure 17c) is employed to help control the working distance from the UAV to the surface of the pier. The measurement range and resolution of the radar map are about 0.7–6.0 m, and 0.5 m, respectively. After obtaining the image data and finishing the 3D reconstruction, it is found that the final average working distances of the three flight paths are 1.03 m,



FIGURE 17 Test process of UAV operation and crack measurement

1.61 m, and 1.90 m, respectively. Besides the UAV inspection, inspection using a hand-held digital single-lens reflex camera (DSLR) is conducted for comparison. The path of DSLR is similar to that of a UAV, and the average working distance is 2.39 m. Important test parameters are presented in Table 2, where two key parameters of the test are computed, that is, the required image number N_r , and the width of narrowest detectable crack W_{\min} .

The value of N_r is obtained by the first equation of Equations (3) and (5). For the four tests, N_r equals 10, 21, 13, and 27, respectively. This parameter works as an important reference for on-site shooting, representing the number of images that should be shot when the UAV flies around in the ideal case. The required image number N_r is computed under the assumption that each photo is shot with the same working distance and the camera directions are right against the pier center. However, in the field test, especially when taking images using the UAV, the above requirements can

**TABLE 2** Test parameters

Camera and lens	UAV (X5S)			Test 4, DSLR (Canon 1D Mark III)
	Test 1, further	Test 2, closer	Test 3, intermediate	
Focal length f , mm	15	15	15	80
Horizontal imaging angle γ	61.93°	61.93°	61.93°	25.36°
Average working distance l , m ($\approx u$)	1.90	1.03	1.61	2.39
Average image distance v , mm	30.76	31.25	30.85	72.68
Computed central angle θ	36.07°	16.28°	28.18°	13.23°
Computed required image number N_r	9.98 \approx 10	22.12 \approx 21	12.78 \approx 13	27.20 \approx 27
Shot and selected image number N_s	19	31	22	30
N_s/N_r	1.9	1.4	1.7	1.1
P_c , pixel/mm	293	293	293	152
Width of the narrowest crack detectable W_{\min} , mm	1.29	0.69	1.09	0.57

Abbreviations: DSLR, digital single-lens reflex camera; UAV, unmanned aerial vehicle.

not be completely satisfied. Therefore, a few more images (the number is N_s) than the computed required image number (N_r) are actually shot and selected for crack detection and 3D reconstruction. The rate of N_s/N_r is about 1.4–1.9 for the three tests using the UAV. In comparison, the hand-held shot using the DSLR has much better control of the camera location and direction. Therefore, the number of actual shots and selected images is quite close to the computed required image number N_r , and the rate is about 1.1. If the number of selected images for modeling is less, the reconstruction fails.

When the crack that is 3 pixels in width is assumed to be the narrowest detectable, the width of the narrowest detectable crack for the four tests is computed as 1.29 mm, 0.69 mm, 1.09 mm, and 0.57 mm, respectively.

6.4 | Image data and preprocessing

1. Selected image collections—The images for 3D reconstruction and crack detection of the four tests are presented in Figures 18–21; the numbers of image sequences are 19, 31, 22, and 30, respectively.
2. Result of 3D scene reconstruction—3D scene reconstruction is conducted using the methods listed in Section 4.2. The sparse point cloud and recovered camera location of all four tests are presented in Figures 22 and 23. Figure 22 shows the axonometric view of the recovered model of Test 1, and Figure 23 shows the top view of all four models. The recovered models of all four tests are in good agreement with the actual situation, because the cross sections of the pier surfaces shown in the top view are complete and accurate circles. The triangular surface meshing is carried out by the sparse point cloud models.

3. Crack detection using DIP—Crack detection is conducted using the methods presented in Section 4.1. The crack images are selected from the image sequences. The numbers of crack images for the four tests are 6, 8, 6, and 9, respectively. The processing details and obtained crack width feature pair sequences are presented in Figure 24, where the crack is segmented, and one of the crack segments is being identified as two edge lines and one skeleton line.

6.5 | Crack projection process

The obtained crack width feature pair sequences are projected onto the 3D triangular surface model, as presented in Figure 25. After size correction of the 3D triangular surface model, the real width of the crack can be obtained by calculating the distance between the two projected crack width points. Figure 26 shows the projection result, where the solid lines on the 3D surface model are the projected crack skeletons. The shape of the projected cracks coincides with the shape of the real cracks, as shown in the partially enlarged drawing in Figure 26. Detection of large-area cracks contained in multiple crack images are realized, as shown in the unfolding region of the surface model, where true and accurate crack information on four crack images from #6 to #9 is combined.

6.6 | Result of crack assessment

The unfolded crack nephograms of all four tests are presented in Figure 27, which are drawn by connecting the projected crack skeleton points. The nephogram color represents the width of the crack. Among the four nephograms, the crack shapes of Test 2 and Test 4 are complete and contain almost all the narrow cracks. The nephograms of Test 1 and Test 3 lack a few narrow cracks because the working distances in Test 1 and

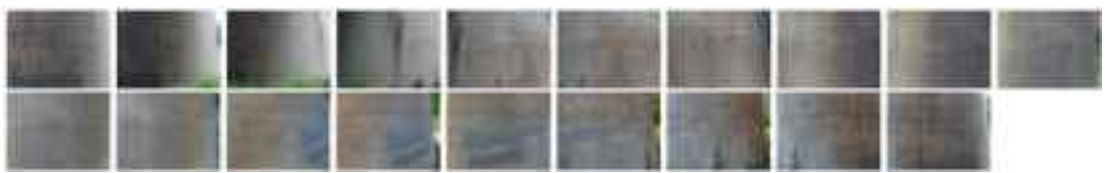


FIGURE 18 Image data for Test 1 (further distance from the UAV)



FIGURE 19 Image data for Test 2 (closer distance from the UAV)



FIGURE 20 Image data for Test 3 (intermediate distance from the UAV)



FIGURE 21 Image data for Test 4 by a digital single-lens reflex camera

Test 3 are longer, and some of the narrowest cracks exceeded the detection capability. Crack widths of the 15 points are measured manually, and the point locations are marked on the nephogram of Test 4. The error analysis is discussed in the next subsection.

Furthermore, the detected crack in the inspection zone can be marked in the entire surface model of the pier to achieve global crack localization. Here, 70 more images shot around the pier using the same UAV system with a longer working distance, together with the image data of Test 2, are adopted for the 3D scene reconstruction. The same crack projection process is implemented and the crack

nephogram is marked on the 3D surface model, as presented in Figure 28. The entire surface model is more elaborate in the inspection zone and rougher in the noninspection zone, but the overall quality is fully available for the global localization of the crack. This global crack localization model can be further used for structural safety analysis or long-term monitoring.

6.7 | Error analysis

The results of the measured and computed crack width of the 15 points are listed in Table 3. The absolute error is obtained



FIGURE 22 Sparse point cloud and recovered camera location for Test 1 (axonometric view)

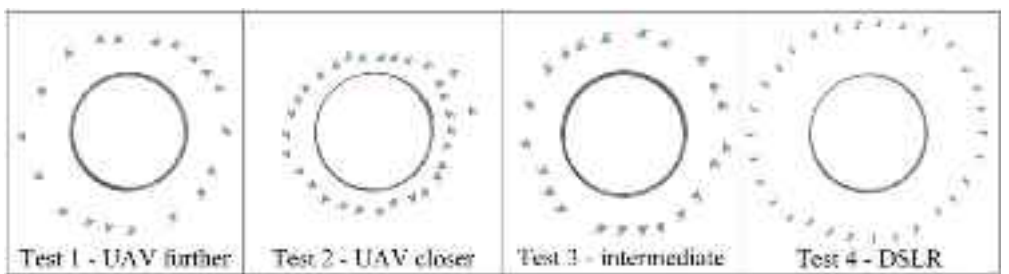


FIGURE 23 Sparse point cloud and recovered camera location for the four tests (top view)

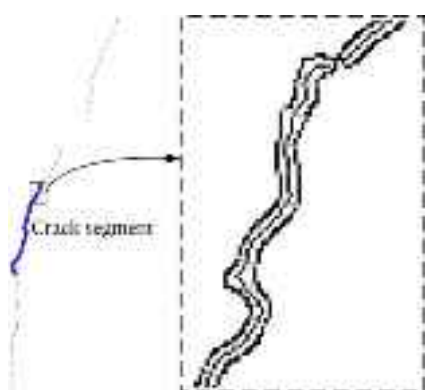


FIGURE 24 Crack detection using a 2D digital image

by subtracting the assessed crack width from the measured width, and the relative error is obtained by dividing the absolute error by the measured crack width. For Test 1 and Test 3, the working distances are further, so some of the narrowest cracks may not be detected.

Obviously, error results for different widths of cracks vary. For Test 2, the mean of the relative error of cracks 1# to 15# is 29%. If the narrowest crack, 15#, is excluded, the mean of the relative error reduces sharply to 13%. For Test 4, a similar phenomenon exists, and the mean of the relative error of cracks 1# to 14# is only 1%. Furthermore, by observing the variation in the relative errors of different crack widths, it is found that

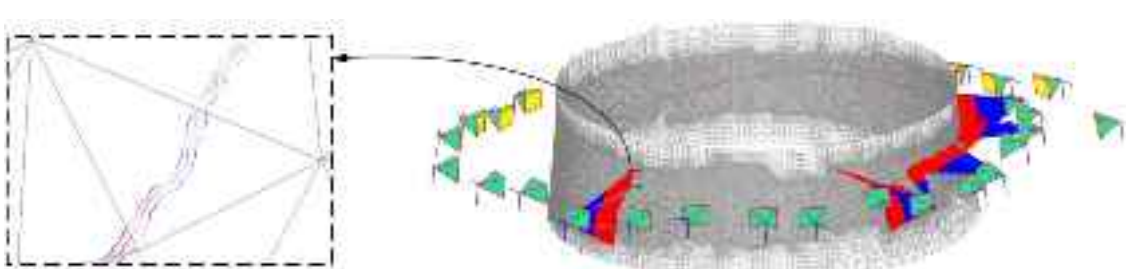


FIGURE 25 Projection process of Test 2

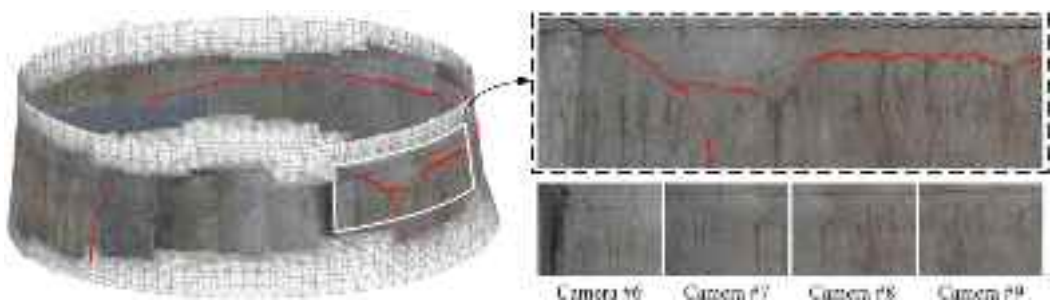


FIGURE 26 Projection result of Test 2

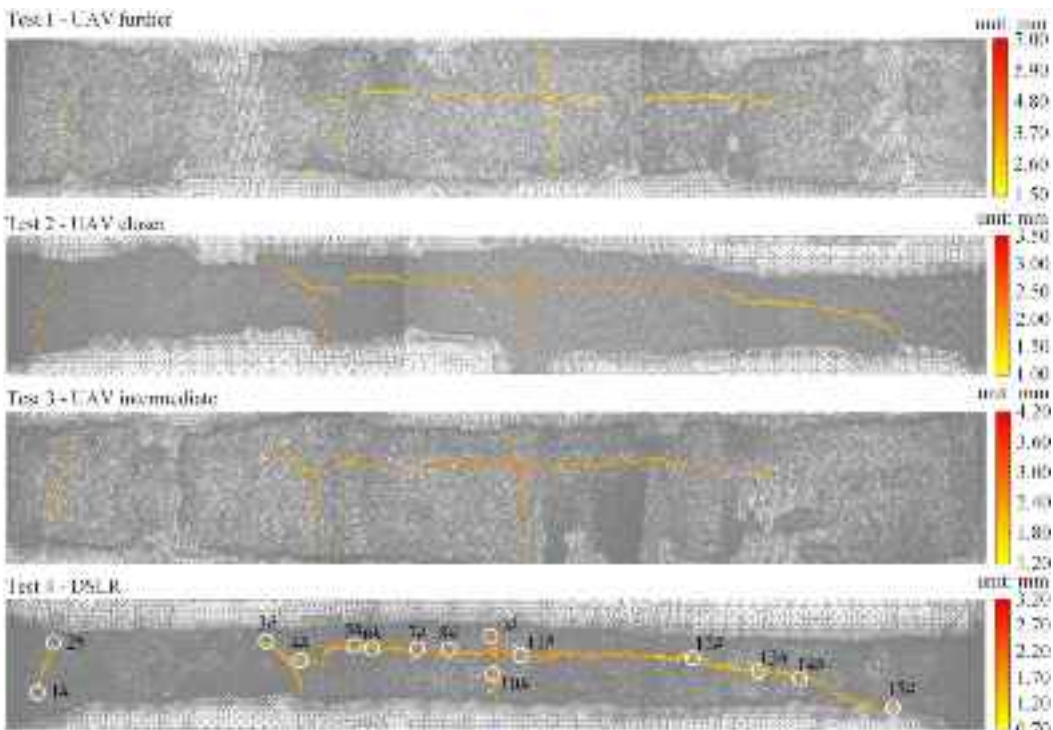


FIGURE 27 Unfolded crack nephogram

the wider the crack, the smaller the relative error. Here, the judgment of whether a crack is wider or narrower is relative to the narrowest detectable crack W_{\min} listed in Table 2. The standard deviation of the relative errors of three UAV tests is similar, from 26% to 29%, when the narrowest cracks are excluded. This value is almost twice as much as that obtained in Test 4—12%—that is, the hand-held DSLR test. The analysis results indicate that the employed UAV performs more unstably than the hand-held DSLR when taking crack images.

Figure 29 presents the relationship between the absolute value of the relative error and the quotient of the assessed crack width and W_{\min} . Because W_{\min} represented the real length of 1 pixel in the images, this quotient represents the number of pixels along the crack width direction. In Figure 29, all four tests show similar distribution patterns—that when the quotient becomes larger, the absolute value of the relative error reduces rapidly. The fitting curves (with 95% confidence interval) of the relative errors of Tests 1–3 (the results of a UAV) and Test 4 (the results of DSLR) almost overlap,



FIGURE 28 Crack localization and nephogram for the entire pier surface model



TABLE 3 Comparison results of the assessed and measured crack width

Assessed crack width using UAV (X5S)										Assessed crack width using DSLR					
Test 1, further					Test 2, closer					Test 3, intermediate			Test 4 (Canon 1D Mark III)		
Measured crack width, mm	Width, mm	Absolute error, mm	Relative error, %	Width, mm	Absolute error, mm	Relative error, %	Width, mm	Absolute error, mm	Relative error, %	Width, mm	Absolute error, mm	Relative error, %	Width, mm	Absolute error, mm	Relative error, %
1#	2.50	2.75	+0.25	10	2.51	+0.01	0	2.61	+0.11	4	1.81	-0.69	-28		
2#	1.30	2.57	+1.27	98	1.58	+0.28	22	2.05	+0.75	58	1.26	-0.04	-3		
3#	1.80	2.55	+0.75	42	1.84	+0.04	2	2.24	+0.44	24	1.69	-0.11	-6		
4#	2.40	2.69	+0.29	12	2.31	-0.09	-4	2.37	-0.03	-1	2.18	-0.22	-9		
5#	2.40	3.33	+0.93	39	2.15	-0.25	-10	2.88	+0.48	20	2.34	-0.06	-3		
6#	2.50	3.09	+0.59	24	2.48	-0.02	-1	2.99	+0.49	20	2.49	-0.01	0		
7#	2.30	3.66	+1.36	59	2.65	+0.35	15	3.29	+0.99	43	2.40	+0.10	4		
8#	2.40	3.85	+1.45	60	2.38	-0.02	-1	2.28	-0.12	-5	2.57	+0.17	7		
9#	2.60	3.65	+1.05	40	2.23	-0.37	-14	2.56	-0.04	-2	2.58	-0.02	-1		
10#	2.40	2.61	+0.21	9	2.09	-0.31	-13	2.30	-0.10	-4	2.52	+0.12	5		
11#	1.80	2.49	+0.69	38	1.97	+0.17	9	2.68	+0.88	49	1.82	+0.02	1		
12#	1.30	2.68	+1.38	106	2.45	+1.15	88	2.26	+0.96	74	1.59	+0.29	22		
13#	1.60	2.45	+0.85	53	2.29	+0.69	43	/	/	/	1.66	+0.06	4		
14#	1.20	/	/	/	1.75	+0.55	46	/	/	/	1.46	+0.26	22		
15#	0.45	/	/	/	1.57	+1.12	249	/	/	/	1.16	+0.71	158		
Mean of relative error	1#–13#: 45%					1#–15#: 29%					1#–15#: 12%				
Standard deviation of relative error	1#–13#: 29%					1#–15#: 65%					1#–15#: 41%				
	1#–14#: 28%					1#–12#: 26%					1#–14#: 12%				

Abbreviations: DSLR, digital single-lens reflex camera; UAV, unmanned aerial vehicle.

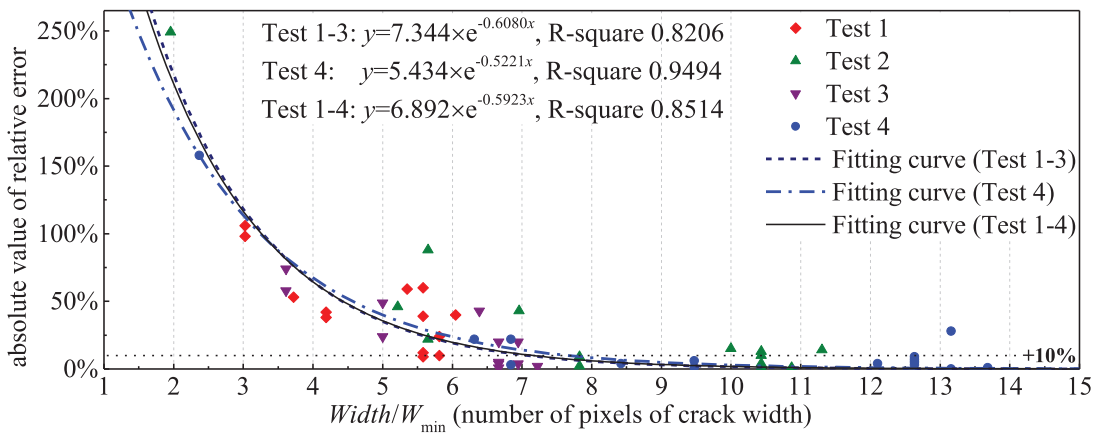


FIGURE 29 Relationship of the absolute value of relative error to $Width/W_{\min}$

indicating that the error low of the test using a UAV is similar to that of the test that used a DSLR. The R-square factors (the coefficient of determination) of three fitting curves are all above 0.82 (1.00 means there is perfect fitting). From the fitting curves of the absolute value of the relative error, it is seen that when the measured crack width is more than 7 pixels, it is possible for the absolute value of the relative error to be smaller than 10%.

7 | CONCLUSION

This paper proposes a systematic surface crack assessment methodology for bridge piers using a UAV, which corrects both the perspective distortion and geometry distortion by nonflat structural surfaces, and realizes crack localization. Field test investigations of crack assessment of a bridge pier using a UAV are carried out for illustration, validation, and error analysis of the proposed methodology, and the following conclusions are safely drawn:

1. The parameter of the required image number N_r , which represents the number of images that should be acquired when the UAV flies around the pier under ideal conditions, serves as an important reference for on-site shooting. For field tests or practical engineering applications, a few more images about 1.4–1.9 times N_r are suggested to be shot considering the instability when taking images using a UAV.
2. For the test of a UAV with a shorter working distance, the detected crack shapes are complete and contain almost all the narrow cracks. The shape of the projected cracks on the 3D surface model coincides with the shape of the real cracks, thereby verifying the effectiveness of the proposed methods in crack identification and shape correction.

3. Error analysis of the test results indicates that the relative error of crack detection using the proposed methods and hand-held DSLR have a similar distribution pattern. But the former method performs more unstably than the latter one with larger standard deviations of relative error.

The outstanding advantages of the proposed methodology are shown in the following aspects:

1. Both the perspective distortion and the geometry distortion by nonflat structural surfaces in the crack images are corrected after the projection. The nonflat structural surfaces can have any kind of surface geometry. The corrected crack objects are in real and original 3D shape, and the crack width is accurately calculated after the correction.
2. Global localization of the detected cracks is achieved, and the relative positions of the detected cracks are marked on the 3D model of the bridge pier.
3. Detection of large-area cracks is realized by projecting and stitching cracks on different images into the same 3D model.

The proposed methodology in this paper supplies a convenient and reliable solution for the surface crack assessment methodology for bridge piers using a UAV and offers significant potential for practical implementation. Some more developments need to be carried out in the future to improve the performance of this method, which include the following:

1. The section for image data acquisition and the field test in this study consider the detection of circumferential cracks rather than vertically aligned cracks. Though the proposed crack projection method can be adopted to correct cracks in any direction, fine inspection and 3D reconstruction of all the bridge piers require a more efficient method.



2. More kinds of UAV systems with longer focal lengths and different values of P_c need to be tested to improve the accuracy of crack width calculation.

Meanwhile, by introducing and combining other automatic crack assessment methods, such as crack detection based on ConvNets, and UAV automatic control and inspection methods based on GPS or local base stations, the integrated method may achieve full automation and eliminate manual operations completely.

ACKNOWLEDGMENT

This research was supported by the National Natural Science Foundation of China (grant no. 51978376, 51725803). The authors express their sincere appreciation for their support.

REFERENCES

- Abdel-Qader, I., Abudayyeh, O., & Kelly, M. E. (2003). Analysis of edge-detection techniques for crack identification in bridges. *Journal of Computing in Civil Engineering*, 17(4), 255–263.
- Adhikari, R. S., Moselhi, O., & Bagchi, A. (2014). Image-based retrieval of concrete crack properties for bridge inspection. *Automation in Construction*, 39, 180–194.
- Alcantarilla, P. F., Bartoli, A., & Davison, A. J. (2012). KAZE features. In A. Fitzgibbon, S. Lazebnik, P. Perona, Y. Sato, & C. Schmid (Eds.), *Computer vision—ECCV 2012. ECCV 2012. Lecture notes in computer science* (pp. 214–227). Berlin: Springer.
- Amezquita-Sánchez, J., & Adeli, H. (2015). Feature extraction and classification techniques for health monitoring of structures. *Scientia Iranica*, 22(6), 1931–1940.
- Barnes, C., Shechtman, E., Finkelstein, A., & Goldman, D. B. (2009). PatchMatch: A randomized correspondence algorithm for structural image editing. *ACM Transactions on Graphics (ToG)*, 28(3), 24.
- Cha, Y. J., Choi, W., & Büyüköztürk, O. (2017). Deep learning-based crack damage detection using convolutional neural networks. *Computer-Aided Civil and Infrastructure Engineering*, 32(5), 361–378.
- Cheng, J., Leng, C., Wu, J., Cui, H., & Lu, H. (2014). Fast and accurate image matching with cascade hashing for 3D reconstruction. In *2014 IEEE Conference on Computer Vision and Pattern Recognition* (pp. 1–8). Washington, DC: IEEE.
- Ellenberg, A., Kontsos, A., Moon, F., & Bartoli, I. (2016). Bridge related damage quantification using unmanned aerial vehicle imagery. *Structural Control and Health Monitoring*, 23(9), 1168–1179.
- Ericson, C. (2004). *Real-time collision detection*. Boca Raton: CRC Press.
- Fujita, Y., & Hamamoto, Y. (2011). A robust automatic crack detection method from noisy concrete surfaces. *Machine Vision and Applications*, 22(2), 245–254.
- Huang, J., Tian, P., Xu, Y., & Xing, C. (2017). An improved adaptive width template method for crack detection of nuclear containments. *Journal of Surveying Engineering*, 143(4), 04017016.
- Jahanshahi, M. R., & Masri, S. F. (2012). Parametric performance evaluation of wavelet-based corrosion detection algorithms for condition assessment of civil infrastructure systems. *Journal of Computing in Civil Engineering*, 27(4), 345–357.
- Jancosek, M., & Pajdla, T. (2014). Exploiting visibility information in surface reconstruction to preserve weakly supported surfaces. *International Scholarly Research Notices*, 2014, 798595.
- Kang, D., & Cha, Y. J. (2018). Autonomous UAVs for structural health monitoring using deep learning and an ultrasonic beacon system with geo-tagging. *Computer-Aided Civil and Infrastructure Engineering*, 33(10), 885–902.
- Khaloo, A., Lattanzi, D., Cunningham, K., Dell'Andrea, R., & Riley, M. (2018). Unmanned aerial vehicle inspection of the Placer River Trail Bridge through image-based 3D modelling. *Structure and Infrastructure Engineering*, 14(1), 124–136.
- Khan, F., Ellenberg, A., Mazzotti, M., Kontsos, A., Moon, F., Pradhan, A., & Bartoli, I. (2015). Investigation on bridge assessment using unmanned aerial systems. *Structures Congress*, 2015, 404–413.
- Kim, H., Ahn, E., Shin, M., & Sim, S.-H. (2019). Crack and noncrack classification from concrete surface images using machine learning. *Structural Health Monitoring*, 18, 725–738.
- Lee, B. Y., Kim, Y. Y., Yi, S.-T., & Kim, J.-K. (2013). Automated image processing technique for detecting and analysing concrete surface cracks. *Structure and Infrastructure Engineering*, 9(6), 567–577.
- Lei, B., Wang, N., Xu, P., & Song, G. (2018). New crack detection method for bridge inspection using UAV incorporating image processing. *Journal of Aerospace Engineering*, 31(5), 04018058.
- Li, S., Zhao, X., & Zhou, G. (2019). Automatic pixel-level multiple damage detection of concrete structure using fully convolutional network. *Computer-Aided Civil and Infrastructure Engineering*, 34(7), 616–634.
- Liu, Y., Cho, S., Spencer, B. F., & Fan, J. S. (2014). Automated assessment of cracks on concrete surfaces using adaptive digital image processing. *Smart Structures and Systems*, 14(4), 719–741.
- Liu, Y. F., Cho, S., Spencer, B. F., Jr., & Fan, J. S. (2016). Concrete crack assessment using digital image processing and 3D scene reconstruction. *Journal of Computing in Civil Engineering*, 30(1), 04014124.
- Lowe, D. G. (2004). Distinctive image features from scale-invariant keypoints. *International Journal of Computer Vision*, 60(2), 91–110.
- Maeda, K., Takahashi, S., Ogawa, T., & Haseyama, M. (2019). Convolutional sparse coding-based deep random vector functional link network for distress classification of road structures. *Computer-Aided Civil and Infrastructure Engineering*, 34(8), 654–676.
- Metni, N., & Hamel, T. (2007). A UAV for bridge inspection: Visual servoing control law with orientation limits. *Automation in Construction*, 17(1), 3–10.
- Morgenthal, G., & Hallermann, N. (2014). Quality assessment of unmanned aerial vehicle (UAV) based visual inspection of structures. *Advances in Structural Engineering*, 17(3), 289–302.
- Moulou, P., Monasse, P., & Marlet, R. (2012). Adaptive structure from motion with a contrario model estimation. In K. M. Lee, Y. Matsushita, J. M. Rehg, & Z. Hu (Eds.), *Computer vision—ACCV 2012. ACCV 2012. Lecture notes in computer science* (pp. 257–270). Berlin: Springer.
- Nishikawa, T., Yoshida, J., Sugiyama, T., & Fujino, Y. (2012). Concrete crack detection by multiple sequential image filtering. *Computer-Aided Civil and Infrastructure Engineering*, 27(1), 29–47.
- Ou, J., & Li, H. (2010). Structural health monitoring in mainland China: Review and future trends. *Structural Health Monitoring*, 9(3), 219–231.
- Qarib, H., & Adeli, H. (2014). Recent advances in health monitoring of civil structures. *Scientia Iranica*, 21(6), 1733–1742.



- Rashidi, A., Dai, F., Brilakis, I., & Vela, P. (2013). Optimized selection of key frames for monocular videogrammetric surveying of civil infrastructure. *Advanced Engineering Informatics*, 27, 270–282.
- Reagan, D., Sabato, A., & Nierzrecki, C. (2018). Feasibility of using digital image correlation for unmanned aerial vehicle structural health monitoring of bridges. *Structural Health Monitoring*, 17(5), 1056–1072.
- Sankarasrinivasan, S., Balasubramanian, E., Karthik, K., Chandrasekar, U., & Gupta, R. (2015). Health monitoring of civil structures with integrated UAV and image processing system. *Procedia Computer Science*, 54, 508–515.
- Sinha, S. K., & Fieguth, P. W. (2006). Segmentation of buried concrete pipe images. *Automation in Construction*, 15(1), 47–57.
- Sonka, M., Hlavac, V., & Boyle, R. (1999). *Image processing, analysis, and machine vision*. Boston: Springer.
- Vaghefi, K., Oats, R. C., Harris, D. K., Ahlborn, T. M., Brooks, C. N., Endsley, K. A., ... Dobson, R. (2011). Evaluation of commercially available remote sensors for highway bridge condition assessment. *Journal of Bridge Engineering*, 17(6), 886–895.
- Vu, H.-H., Labatut, P., Pons, J.-P., & Keriven, R. (2012). High accuracy and visibility-consistent dense multiview stereo. *IEEE Transactions on Pattern Analysis and Machine Intelligence*, 34(5), 889–901.
- Wang, X., & Hu, Z. (2017). Grid-based pavement crack analysis using deep learning. In *2017 4th International Conference on Transportation Information and Safety (ICTIS)* (pp. 917–924). Washington, DC: IEEE.
- Xu, Y., Li, S., Zhang, D., Jin, Y., Zhang, F., Li, N., & Li, H. (2018). Identification framework for cracks on a steel structure surface by a restricted Boltzmann machines algorithm based on consumer-grade camera images. *Structural Control and Health Monitoring*, 25(2), e2075.
- Yang, X., Li, H., Yu, Y., Luo, X., Huang, T., & Yang, X. (2018). Automatic pixel-level crack detection and measurement using fully convolutional network. *Computer-Aided Civil and Infrastructure Engineering*, 33(12), 1090–1109.
- Yeum, C. M., & Dyke, S. J. (2015). Vision-based automated crack detection for bridge inspection. *Computer-Aided Civil and Infrastructure Engineering*, 30(10), 759–770.
- Zhang, A., Wang, K. C., Li, B., Yang, E., Dai, X., Peng, Y., ... Chen, C. (2017). Automated pixel-level pavement crack detection on 3D asphalt surfaces using a deep-learning network. *Computer-Aided Civil and Infrastructure Engineering*, 32(10), 805–819.
- Zhu, Z. H., Fu, J. Y., Yang, J. S., & Zhang, X. M. (2016). Panoramic image stitching for arbitrarily shaped tunnel lining inspection. *Computer-Aided Civil and Infrastructure Engineering*, 31(12), 936–953.
- Zisserman, A. (2003). *Multiple view geometry in computer vision*. Cambridge, UK: Cambridge University Press.

How to cite this article: Liu Y-F, Nie X, Fan J-S, Liu X-G. Image-based crack assessment of bridge piers using unmanned aerial vehicles and three-dimensional scene reconstruction. *Comput Aided Civ Inf*. 2020;35: 511–529. <https://doi.org/10.1111/mice.12501>